Available online at www.sciencedirect.com
ScienceDirect
Acta Materialia 58 (2010) 4424–4431
Acta MATERIALIA
www.elsevier.com/locate/actamat

Low thermal conductivity without oxygen vacancies in equimolar $YO_{1.5} + TaO_{2.5}$- and $YbO_{1.5} + TaO_{2.5}$-stabilized tetragonal zirconia ceramics

Yang Shen [a], Rafael M. Leckie [b], Carlos G. Levi [b], David R. Clarke [a,*]

[a] School of Engineering and Applied Sciences, Harvard University, Cambridge, MA 02138, USA
[b] Materials Department, College of Engineering, University of California, Santa Barbara, CA 93106, USA

Received 7 December 2009; received in revised form 9 March 2010; accepted 25 April 2010
Available online 18 May 2010

Abstract

A narrow range of composition exists along both the ZrO_2–$YTaO_4$ and ZrO_2–$YbTaO_4$ quasi-binaries over which the tetragonal zirconia phase can be retained on cooling. Unlike other stabilized zirconia materials which have low thermal conductivity as a result of phonon scattering by oxygen vacancies, these compositions do not contain oxygen vacancies and yet an equimolar $YO_{1.5} + TaO_{2.5}$ composition has been reported to also exhibit low thermal conductivity [1]. We find that zirconia compositions along the quasi-binaries have low and temperature-independent thermal conductivities, and that the thermal conductivities and their temperature dependence are consistent with a defect scattering model that takes into account a minimum phonon mean free path due to the inter-atomic spacing. Furthermore, the conductivities of the Yb and Y trivalent-doped compositions scale in a predictable manner with atomic site disorder effects on the cation sub-lattice associated with the lighter Y^{3+} ions and the heavier Yb^{3+} and Ta^{5+} ions. The lowest thermal conductivity measured was $\sim$1.4 W mK^{-1} at 900 °C. The low thermal conductivity and phase stability makes these systems promising candidates for low conductivity applications, such as thermal barrier coatings.

Keywords: Low thermal conductivity; Zirconia; Defect models

1. Introduction

The low thermal conductivity of yttria-stabilized zirconia (YSZ) is usually attributed to the high concentration of oxygen vacancies in this material [2–4]. Oxygen vacancies are very effective in scattering phonons, especially at high concentrations (typically 1.9 at.%) in the 8YSZ (7.6 m/o $YO_{1.5}$) composition currently used in the majority of thermal barrier coatings. Alternative compositions, produced by co-doping zirconia with both Y^{3+} and Ta^{5+}, have low thermal conductivity. There is also a report in the literature that a zirconia ceramic composition co-doped with equal amounts of Y^{3+} and Ta^{5+} also exhibits low thermal conductivity [1], although the authors of that report were unable to explain the values of the conductivity based on the models they used. An intriguing feature of these co-doped compositions is that nominally they contain no oxygen vacancies: they incorporate equal concentrations of trivalent (Y^{3+}) and pentavalent (Ta^{5+}) ions, so charge neutrality is satisfied without the introduction of any oxygen vacancies. This is borne out by the very low ionic conductivity of very similar materials co-doped with Nb^{5+} (rather than Ta^{5+}) compared to zirconias containing oxygen vacancies [5].

There exists a range of composition in the Zr–Y–Ta–O system, shown in Fig. 1, over which tough, single-phase materials, sometimes referred to as "non-transformable" zirconias, form [6]. This compositional range is highlighted in green in the figure and corresponds to materials formed by equimolar doping with both Y^{3+} and Ta^{5+} ions. As

* Corresponding author. Tel.: +1 617 495 4140.
E-mail address: clarke@seas.harvard.edu (D.R. Clarke).

1359-6454/$36.00 © 2010 Published by Elsevier Ltd. on behalf of Acta Materialia Inc.
doi:10.1016/j.actamat.2010.04.040

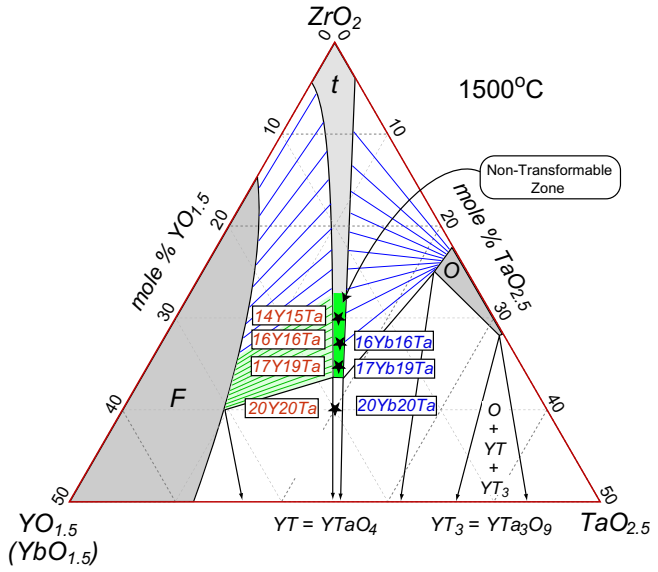

Fig. 1. Isothermal section of the $YO_{1.5}$–$TaO_{2.5}$–ZrO_2 ($YbO_{1.5}$–$TaO_{2.5}$–ZrO_2) phase diagram at 1500 °C. The compositions studied are indicated with pentagrams. The compositional range of the "non-transformable zone" along the ZrO_2–$YTaO_4$ quasi-binary is also indicated.

shown in complementary studies at UCSB, a very similar range of single-phase "non-transformable" zirconias form when Yb^{3+} is used as the co-stabilizer in place of Y^{3+} [7].

In this work we have re-evaluated the thermal conductivity of a range of compositions formed by equal co-doping of Y^{3+} and Ta^{5+} ions, compared them with identical compositions formed using a heavier trivalent ion, Yb^{3+}, in the place of Y^{3+}, and shown that the thermal conductivity can be satisfactorily explained quantitatively using existing defect models for thermal conductivity.

2. Rationale for comparing Y^{3+} and YB^{3+} as the trivalent dopant

Y^{3+} is used in the state-of-the-art thermal barrier coating (TBC) composition (8YSZ) to stabilize the tetragonal form of zirconia. Its selection is largely a consequence of the historical development of stabilized zirconias and the cheaper cost of yttrium relative to other trivalent rare-earth ions that can also be used to stabilize tetragonal zirconia. Of the alternative rare-earth stabilizers, Yb^{3+} is almost the same ionic size as Y^{3+}, is comparable in effectiveness in stabilizing tetragonal zirconia [8] but is almost twice as massive (Table 1). This latter characteristic is of significance because phonon scattering depends on atomic mass as well as the mass differences with other ions in the crystal [9,10].

Table 1
Atomic mass and ionic radius.

Ion	Zr^{4+}	Y^{3+}	Yb^{3+}	Ta^{5+}	O^{2-}
Atomic mass (amu)	91.2	88.9	173.0	180.9	16
Ionic radius (nm)	0.084	0.1019	0.1008	0.068	

3. Compositions studied

A set of compositions shown in Fig. 1 and detailed in Table 2 were prepared to investigate how the thermal conductivity depends on composition within the "non-transformable" tetragonal region of the quasi-binary ZrO_2–$RETaO_4$ and to compare the effects of Y^{3+} vs. Yb^{3+} doping. On the same cation (half-oxide) basis, the composition of the comparable material studied by Raghavan et al. [1] was ZrO_2–16.6 $YO_{1.5}$ + 16.6 $TaO_{2.5}$.

The powders for the ZrO_2–$YO_{1.5}$–$TaO_{2.5}$ specimens were made by reverse co-precipitation using zirconium oxychloride, yttrium nitrate and tantalum chloride precursor solutions. First, solutions of $ZrOCl_2$ and $Y(NO_3)_3$ in deionized (DI) water and solutions of $TaCl_5$ in absolute ethanol were prepared. They were then mixed together immediately before initiating precipitation to prevent the hydrolysis of $TaCl_5$ that occurs in the presence of water. (All chemicals used were from Sigma–Aldrich with a purity of 99.9%.) Once the solutions were mixed, precipitation was initiated by slowly adding the solution, drop by drop, into an ammonia hydroxide solution (the pH value was controlled to be >9 during precipitation) while stirring vigorously. The precipitants were then washed three times, first with DI water and then twice with ethanol. After each wash, the precipitants were ultrasonically re-dispersed into the ethanol solvent. After the final wash, the precipitants were dried under vacuum overnight at 70 °C and then calcined at 700 °C for 2 h to produce a molecularly mixed oxide. The resultant powders were ground with a mortar and pestle and passed through a <325 mesh sieve to eliminate coarse agglomerates. Solid circular pellets were then made by cold, uniaxial pressing the sieved powder at 400 MPa and then sintering for 5 h at 1500 °C. After sintering,

Table 2
Compositions studied in both Zr–Ta–Y–O and Zr–Ta–Yb–O systems.

Sample	Nominal composition	c (nm) (±0.00005)	a (nm) (±0.00005)	c/a ratio	X-ray (g cm^{-3})	Measured (g cm^{-3})	Relative density
14Y–15Ta	$Y_{0.14}Ta_{0.15}Zr_{0.71}O_{2.004}$	0.5243	0.5112	1.0255	6.60	6.45	0.97
16Y–16Ta	$Y_{0.16}Ta_{0.16}Zr_{0.68}O_2$	0.5253	0.5115	1.0269	6.63	6.42	0.97
17Y–19Ta	$Y_{0.17}Ta_{0.19}Zr_{0.64}O_{2.007}$	0.5237	0.5114	1.0241	6.77	6.68	0.98
20Y–20Ta	$Y_{0.2}Ta_{0.2}Zr_{0.6}O_2$	0.5254	0.5119	1.0263	6.79	6.60	0.97
16Yb–16Ta	$Yb_{0.16}Ta_{0.16}Zr_{0.68}O_2$	0.5229	0.5103	1.0248	7.33	7.13	0.97
17Yb–19Ta	$Yb_{0.17}Ta_{0.19}Zr_{0.64}O_{2.007}$	0.5251	0.5104	1.0287	7.47	7.37	0.98
20Yb–20Ta	$Yb_{0.2}Ta_{0.2}Zr_{0.6}O_2$	0.5247	0.5105	1.0278	7.65	6.98	0.91

samples were machined to a size suitable for diffusivity measurements using a surface grinder and diamond files. The density was measured using the Archimedes technique. The ZrO_2–$YbO_{1.5}$–$TaO_{2.5}$ materials were prepared in an identical manner using ytterbium nitrate as the precursor source of ytterbium.

4. Characterization methods

The phase constitution of the materials was analyzed by X-ray diffraction (XRD) on a Philips Xpert powder diffractometer over the range 20–90°. Lattice parameters for the tetragonal samples were determined by slow scan XRD at 70–76° and the X-ray densities for each composition were calculated from the lattice parameters obtained and the chemical composition. Raman spectroscopy was performed at the excitation with an Argon ion laser of 488 nm (Coherent, Santa Clara, CA) and collected with a microscope-based Raman spectroscopy system (Triple monochromator Jobin–Yvon, Edison, NJ.). Raman spectra were employed to complement the XRD characterization since it is more sensitive to the presence of minor quantities of monoclinic zirconia.

Thermal heat capacity measurements up to 900 °C were made on disks, approximately 3 mm in diameter, using a Netzsch Pegasus 404C differential scanning calorimeter. The samples were held in a platinum crucible. The heat capacity measurements were made in conformity to the ASTM standard E1269-95 in an argon atmosphere.

The thermal diffusivity measurements were made with a commercial thermal flash system (Anter Flashline 3000) from 35 °C up to 900 °C. The instrument employs a high-speed xenon flash lamp to illuminate the front of the sample and records the corresponding rise in the backside temperature with an infrared detector. For the thermal diffusivity measurements, the samples were machined to a diameter of 7 mm with a thickness of 1 mm, ensuring co-planarity of both flat surfaces. To minimize radiative transport through the samples, they were rendered opaque by depositing a thin Ti layer of 10 nm followed by a Pt layer of 740 nm on both sides by electron beam physical vapor deposition. A layer of colloidal aerosol of carbon of 10 μm was then sprayed on both sides to ensure maximum absorption and emission. The thermal diffusivity was determined using the correction described by Clarke and Taylor [11]. The thermal conductivity, κ, of each sample was then calculated from the density (ρ), thermal diffusivity (α) and heat capacity (C_P) with the relationship:

$$\kappa = \rho C_P \alpha \tag{1}$$

For any residual porosity (ϕ) present in the sample, the thermal conductivity was further corrected with Maxwell's relation [12] as:

$$\kappa_{dense} = \kappa_{measured} \frac{1}{(1 - 1.5\varphi)} \tag{2}$$

5. Results

As indicated by the XRD patterns in Fig. 2, all three compositions of the non-transformable $YO_{1.5}$–$TaO_{2.5}$–ZrO_2 material had the tetragonal crystal structure. Extra peaks on the shoulders of the tetragonal zirconia peaks at 29.5°, 33.9° and 49.3° were observed in the spectrum for the 20Y–20Ta sample. These were assigned to monoclinic $YTaO_4$ precipitated from the tetragonal major phase. This indicated, as expected from the phase diagram, that this particular composition is a two-phase mixture of zirconia and $YTaO_4$. Interestingly, Raman spectra of these four samples were almost the same with no sign of any presence of monoclinic zirconia phase. Consistent changes in the lattice parameters were observed by the consistent shifts of peaks with composition, as illustrated by the dashed lines superimposed in Fig. 2.

5.1. Specific heat capacity

The variation in heat capacity with temperature for the two series of samples is shown in Fig. 3. For the $YO_{1.5}$–$TaO_{2.5}$–ZrO_2 system, the values exhibited little variation over the solid solution range from room temperature to 1000 °C (the limit of current measurements). No consistent trend could be observed with the increasing concentration of dopants of the heavier Ta^{5+} ions except for the anomalous increase observed in the 20Y–20Ta samples. The difference was <4%, still within the scatter in data obtained by differential scanning calorimetry. More consistent was the decrease in heat capacity with increasing amount of heavy ions observed in the $YbO_{1.5}$–$TaO_{2.5}$–ZrO_2 system. Theoretical estimations were also performed on these compositions by using the Kubaschewski–Alcock–Kellog mixing rules [13], based on the specific heat of an ionic

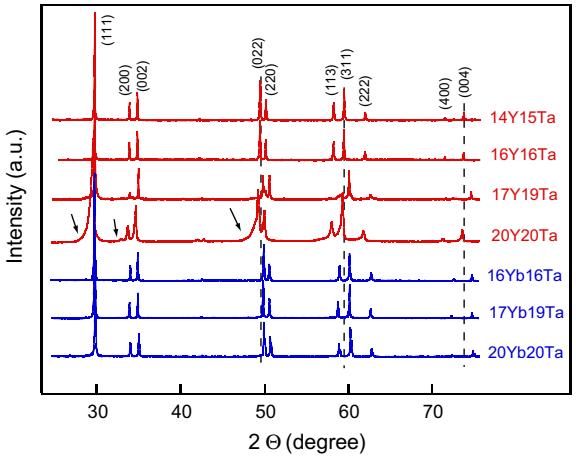

Fig. 2. X-ray diffraction patterns of the compositions studied. On the spectrum for the 20Y–20Ta sample, extra peaks on the shoulders of the peaks at 29.5°, 33.9° and 49.3° were indicated by arrows and assigned to monoclinic $YTaO_4$ precipitated from the tetragonal major phase. Also indicated by dash lines are the consistent shifts of certain peaks with composition.

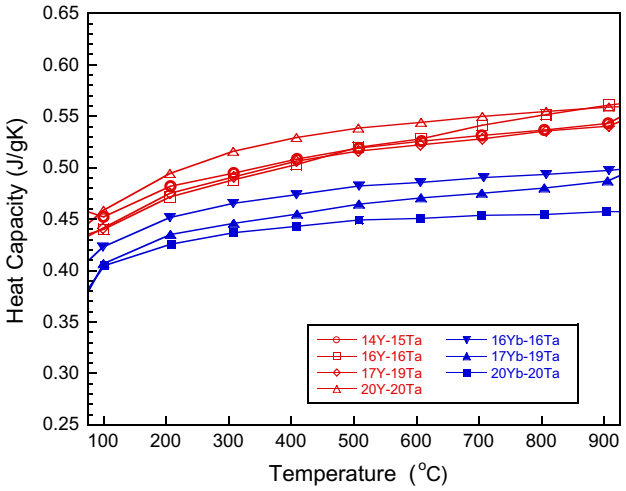

Fig. 3. Specific heat capacities as a function of temperature for the $YO_{1.5}$–$TaO_{2.5}$–ZrO_2 system (red in color and hollow markers) and $YbO_{1.5}$–$TaO_{2.5}$–ZrO_2 system (blue in color and solid markers). (For interpretation of the references to color in this figure legend, the reader is referred to the web version of this article.)

compound being the sum of the contributions of the individual cations and anions in the composition. The maximum deviation of measured values from those calculated was 3% for the 20Y–20Ta samples.

5.2. Thermal diffusivity

The variation of thermal diffusivity with temperature for the two series of compositions is shown in Fig. 4. The thermal diffusivity decreases monotonically with increasing temperature. Also, overall, the $YbO_{1.5}$–$TaO_{2.5}$–ZrO_2 materials consistently exhibited lower thermal diffusivity than the $YO_{1.5}$–$TaO_{2.5}$–ZrO_2 materials.

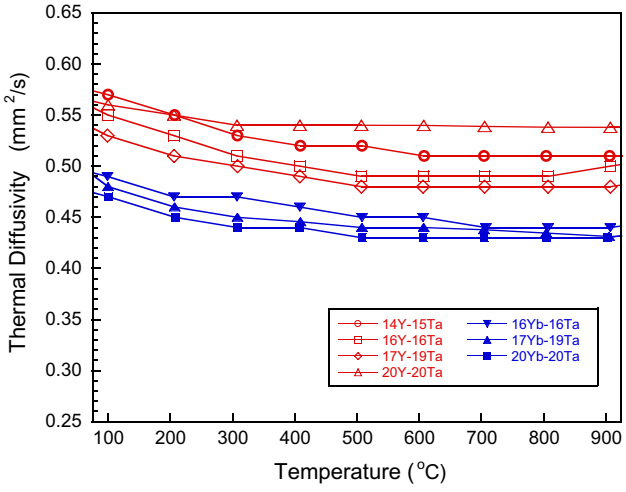

Fig. 4. Temperature dependence of the thermal diffusivity for the $YO_{1.5}$–$TaO_{2.5}$–ZrO_2 system (red in color and hollow markers) and $YbO_{1.5}$–$TaO_{2.5}$–ZrO_2 system (blue in color and solid markers). (For interpretation of the references to color in this figure legend, the reader is referred to the web version of this article.)

5.3. Thermal conductivity

The temperature dependences of thermal conductivities for the two series of materials are shown in Fig. 5a. For comparison, the thermal conductivity of a typical, fully dense ZrO_2–7.6 $YO_{1.5}$ composition is also shown. In contrast with the co-doped compositions, it varies with temperature from 2.9 down to ~2.5 $Wm\,K^{-1}$ over the same temperature range.

Almost temperature-independent thermal conductivities were observed over the temperature range measured, with the Yb compositions exhibiting a slight increase with temperature. In addition, there is a consistent decrease in thermal conductivity with increasing concentration of $(Yb^{3+} + Ta^{5+})$ dopant levels over the same temperature range.

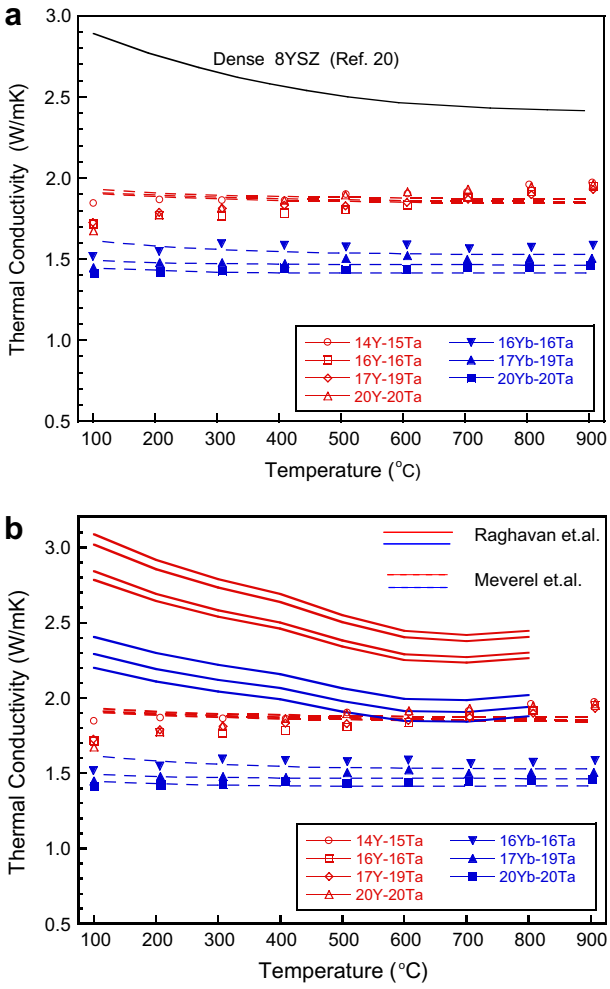

Fig. 5. (a) Temperature dependence of the thermal conductivity for the $YO_{1.5}$–$TaO_{2.5}$–ZrO_2 system (red hollow symbols) and $YbO_{1.5}$–$TaO_{2.5}$–ZrO_2 system (blue solid symbols). Also superimposed is the thermal conductivity of dense 8YSZ [20] in the same temperature range. (b) Comparison between the data and two models. The dash lines (Mevrel) through the data are the best regression fit to the data with Eq. (11) and the solid lines (Ragahavan) are the predictions using Eq. (10). (For interpretation of the references to color in this figure legend, the reader is referred to the web version of this article.)

As will be discussed in the following section, the observed reduction of the thermal conductivity is attributed to the effects of atomic mass disorder created by co-doping of ZrO_2 with trivalent and pentavalent ions of different atomic mass. For the $YO_{1.5}$–$TaO_{2.5}$–ZrO_2 system, the highest thermal conductivity observed at 900 °C was ~2 W mK^{-1} – some 20% lower than a baseline stabilized zirconia (8YSZ, ~2.5 W mK^{-1}). Even lower thermal conductivities were achieved in the $YbO_{1.5}$–$TaO_{2.5}$–ZrO_2 system compared with their $YO_{1.5}$–$TaO_{2.5}$–ZrO_2 counterparts. The lowest thermal conductivity of ~1.45 W mK^{-1} was observed for the 20Yb–20Ta sample at 900 °C, which is almost half that of 8YSZ.

6. Discussion

There are four striking features of the data shown in Fig. 5a. The first is that the thermal conductivities of all of the co-doped compositions are lower than that of fully dense 8YSZ. Second, for the same concentration of co-doping, those co-doped with Yb^{3+} exhibit consistently lower thermal conductivity than those in which Y^{3+} was used. Third, although there is little discernible difference in the conductivity with the concentration of Y^{3+}, there is a systematic decrease in conductivity with Yb^{3+} concentration. Fourth, the conductivities of all the compositions were almost independent of temperature up to at least 800 °C.

As mentioned earlier, these very low thermal conductivities probably cannot be produced by oxygen vacancies as they are in 8YSZ since there are nominally no oxygen vacancies. This is substantiated by the measurements of ionic conductivity of Y and Nb co-doped zirconia, which indicate decreasing ionic conductivity as the equimolar composition is approached [5]. Indeed, the authors of that study were unable to make conductivity measurements of the equimolar composition as the conductivities were too low. In addition, the lowest recorded thermal conductivity of any zirconia containing vacancies is ~2 W mK^{-1} [14]. However, as will be shown, these low conductivities can still be produced as a result of scattering from other point defects on the cation sub-lattice, specifically Y^{3+}, Ta^{5+} and Yb^{3+} ions substituting for Zr^{4+} ions on the cation sub-lattice of the tetragonal solid solution.

The reduction in thermal conductivity of a perfect, pure solid by introducing defects was first analyzed by Klemens [9] and then later by Callaway and von Baeyer [15] using the formalism introduced by Callaway [16]. The basis of the models is that point defects scatter phonons in addition to the usual anharmonic scattering amongst them and thereby reduce thermal conductivity by reducing the phonon mean free path. The phonon mean free path, $\Lambda(\omega)$, is then considered to consist of two components: that due to the anharmonic (Umklapp) scattering of the perfect lattice, $\Lambda_I(\omega)$, and a second that accounts for the defect scattering, $\Lambda_D(\omega)$:

$$\frac{1}{\Lambda(\omega)} = \frac{1}{\Lambda_I(\omega)} + \frac{1}{\Lambda_D(\omega)} \tag{3}$$

where they are all a functions of phonon frequency, ω. The thermal conductivity, κ, can then be evaluated from the general expression for thermal conductivity [17]:

$$\kappa = \frac{1}{3}\int_0^{\omega_{\max}} C(\omega,T)v(\omega)\Lambda(\omega,T)d\omega \tag{4}$$

where $C(\omega)d\omega$ is the contribution to the specific heat at constant volume per unit volume of lattice waves in the frequency interval $d\omega$ at ω, and $v(\omega)$ is the phonon group velocity.

At high temperatures, the solution to the Boltzmann transport equation is simplified and the thermal conductivity due to scattering of point defects, κ_D, can then be related to the thermal conductivity of the perfect crystal, κ_I, as [15]:

$$\kappa_D = \kappa_I(1/u)\ \tan^{-1} u \tag{5}$$

where the parameter u has the form

$$u = (k_B\Theta_D/\hbar)(A/CT)^{1/2} \tag{6}$$

Here, $k_B, \Theta_D, \hbar$ are the Boltzmann constant, Debye temperature and Planck's constant, respectively. C is a temperature-independent parameter that characterizes the anharmonic scattering as a function of phonon frequency [15]. The parameter A is a measure of the scattering produced by the point defects, which can be expressed as [9]:

$$A = \frac{\Omega_0}{4\pi v_s^3}\Gamma \tag{7}$$

where v_s is the speed of sound, Ω_0 is the unit cell volume and Γ is the scattering coefficient that explicitly depends on the concentration of defects. For the case of different cations occupying Zr^{4+} lattice sites, the scattering coefficient takes the form:

$$\Gamma_{\text{Zr-site}} = \sum_i x_i\left[\frac{M_i - M_{\text{Zr}}}{M_{\text{Zr}}}\right]^2 \tag{8}$$

where x_i is the concentration of the dopant, i, M_i is their atomic mass and M_{Zr} is the atomic mass of a Zr^{4+} ion.

For high concentration of defects, such as the compositions studied here, the defect scattering is large, leading to the inverse tangent in Eq. (5) approaching an asymptotic value of $\frac{\pi}{2}$, namely

$$tan^{-1}u = \pi/2 \tag{9}$$

The thermal conductivity due to scattering of point defects then takes the form (Eq. (27) of Ref. [15]):

$$\kappa = k_B/[4\pi v_s(\text{ACT})^{1/2}] \tag{10}$$

The above expression for the thermal conductivity is clearly not consistent with our measurements in Fig. 5a since it predicts a distinct $T^{-1/2}$ temperature dependence and we observe little or no temperature dependence.

Part of the disparity between this standard model and experiment is that it doesn't satisfactorily take into account the fact that phonons cannot have a wavelength, and hence phonon mean free path, smaller than the inter-atomic spacing. Therefore, the integral in Eq. (4) must include a cut-off length corresponding to the inter-atomic spacing. This was recognized by Mevrel et al. [14] and, while the equations involved are necessarily more complex, the thermal conductivity can be written analytically as:

$$\kappa = \frac{A}{T}\frac{\omega_0}{\omega_D} arctg\left(\frac{\omega_1}{\omega_0}\right) + \frac{A}{3T_1}\left[\frac{1}{1+\left(\frac{\omega_1}{\omega_0}\right)^2}\right]\left[\left(\frac{\omega_D}{\omega_1}\right)^2 - \frac{\omega_1}{\omega_D}\right] \tag{11}$$

where

$$\omega_0 = \sqrt{\frac{\beta T}{x}}; \quad \omega_1 = \omega_0\sqrt{-\frac{1}{2}+\sqrt{\frac{1}{4}+\left(\frac{\omega'}{\omega_0}\right)^2}} \tag{12}$$

and

$$\omega' = \sqrt{\frac{T_1}{T}}\omega_D$$

The phonon frequency ω_1 is defined as the frequency for which the mean free path $\Lambda(\omega_1) = \Lambda_{min}$ is the inter-atomic spacing; x is the concentration of the point defects and ω_D is the Debye frequency. The parameters A, T_1 and β are not known a priori and so can be used as fitting parameters. If the Debye frequency is unknown it can be estimated from the Young's modulus using the relationship:

$$\omega_D = 0.87(E\Omega/\overline{M})^{1/2}(6\pi^2/\Omega)^{1/3} \tag{13}$$

As the first step in the fitting, since the Debye frequency, ω_D, is not known for these complex compounds, it was estimated from measurements of the Young's modulus of tetragonal $YO_{1.5}$–$TaO_{2.5}$–ZrO_2 ceramics by Kim and Tien [6]. The value for the Debye frequency obtained this way was $\omega_D = 5.45 \times 10^4$ GHz. In the absence of any additional information, it was assumed to be the same for all the compositions studied. The second parameter β is also unknown, so its value was taken to be the same as used by Mevrel et al. [14] in fitting the thermal conductivity of yttria-stabilized zirconia, namely $\beta = 1.5$ K s^{-2}. Regression fitting was then performed on the data in Fig. 5(a), with A and T_1 as free-fitting parameters. The best regression fits to the data for the thermal conductivities of both the $YO_{1.5}$–$TaO_{2.5}$–ZrO_2 and the $YbO_{1.5}$–$TaO_{2.5}$–ZrO_2 systems are shown by the dashed lines through the data in Fig. 5b. The values of the fitting parameters are listed in Table 3. As a check for consistency, the dependence of the fitting parameter A on the inverse square root of mean atomic mass was evaluated (Fig. 6). This has the same atomic mass dependence as proposed by Grimvall [18] for the mass dependence of thermal conductivity.

While our data can be satisfactorily fit with the refined defect model it does not obviously show from the full equations why the thermal conductivity of the Yb^{3+} co-doped compositions depends on Yb^{3+} concentration or the ratio of conductivities one might expect by replacing Y^{3+} with Yb^{3+}. These can be explained by evaluating the scattering coefficient, Γ, for substitution of these ions as well as Ta^{5+} for Zr^{4+} ions. The Y^{3+} has almost the same atomic mass as a Zr^{4+} ion, whereas both Ta^{5+} and Yb^{3+} are much more massive (Table 1). To do this for the compositions we have studied requires accounting for the fact that, although there are three different dopant ions, they cannot each occupy simultaneously the same sites. Thus, the scattering coefficient needs to be corrected. This can be accomplished in terms of the average mass of the ions and the mass of the average unit cell. This can be written for the $YO_{1.5}$–$TaO_{2.5}$–ZrO_2 system as [19]:

$$\Gamma_{YTaZrO} = \frac{1}{3}\left[\frac{\overline{M}_{Zr\text{-site}}}{M_{YTaZrO}}\right]^2 \Gamma_{Zr-site} \tag{14}$$

where $\overline{M}_{Zr\text{-site}}$ is the average atomic mass on the Zr^{4+} cation sites due to the inter-mixing of all the cations and M_{YTaZrO} the average atomic mass of the unit cell. The

Table 3
The fitting parameters for the $YO_{1.5}$–$TaO_{2.5}$–ZrO_2 and the $YbO_{1.5}$–$TaO_{2.5}$–ZrO_2 systems.

	c_d	A (W m^{-1})	T_1 (K)
Y14–Ta15	0.15	2704	500
Y16–Ta16	0.16	2666	488
Y17–Ta19	0.19	2600	457
Yb16–Ta16	0.32	2585	632
Yb17–Ta19	0.36	2502	600
Yb20–Ta20	0.4	2488	563

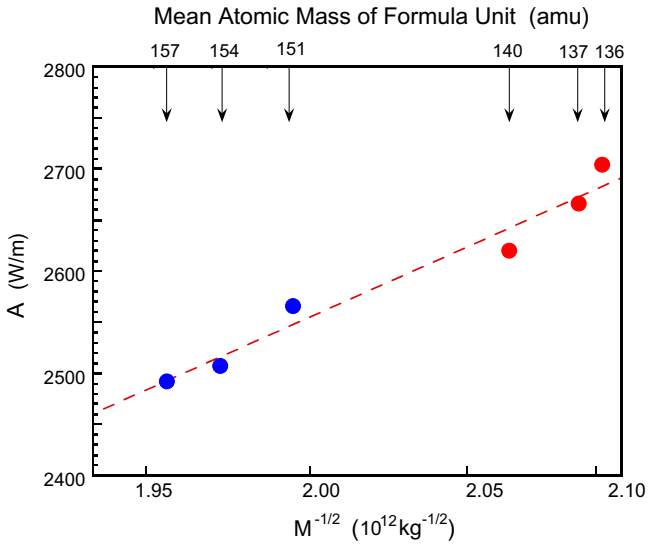

Fig. 6. Demonstration that the fitting parameter, A, varies as the inverse square root of the average atomic mass of the unit cell. $YO_{1.5}$–$TaO_{2.5}$–ZrO_2 (red dots) and the $YbO_{1.5}$–$TaO_{2.5}$–ZrO_2 system (blue dots). (For interpretation of the references to color in this figure legend, the reader is referred to the web version of this article.)

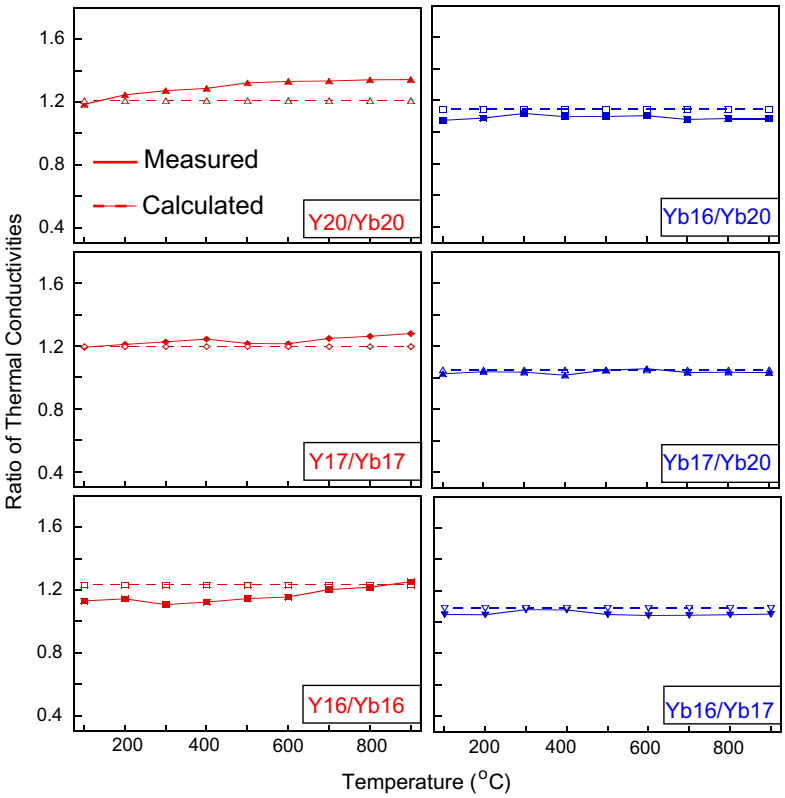

Fig. 7. Variation of the ratios $\kappa_{YTaZrO}/\kappa_{YbTaZrO}$ (red dots and lines) and $\kappa_{YbTaZrO}/\kappa_{YbTaZrO}$ (blue dots and lines) with temperature. Comparisons are made between the thermal conductivities of the samples from the $YO_{1.5}$–$TaO_{2.5}$–ZrO_2 and the $YbO_{1.5}$–$TaO_{2.5}$–ZrO_2 systems with the same dopant concentrations (red, left-hand column) and within the $YbO_{1.5}$–$TaO_{2.5}$–ZrO_2 system for samples with different compositions (right-hand column). (For interpretation of the references to color in this figure legend, the reader is referred to the web version of this article.)

fraction of 1/3 comes about because only one of every three ions in the formula unit $Zr_{1-2x}Y_xTa_xO_2$ is a cation. A similar expression can be written for the Yb-doped system. As the thermal conductivity is inversely proportional to the square root of the phonon scattering coefficient (Eq. (9)), the ratio of the conductivities of the Yb- and Y-doped materials can be simply expressed as:

$$\frac{\kappa_{YTaZrO}}{K_{YbTaZrO}} \propto \left[\frac{\Gamma_{YbTaZrO}}{\Gamma_{YTaZrO}}\right]^{1/2} \tag{15}$$

Comparisons were made both between the two material systems with the same dopant concentrations and within the $YbO_{1.5}$–$TaO_{2.5}$–ZrO_2 system for different compositions. These are shown in Fig. 7. The calculated ratio of thermal conductivities between the two systems agrees very well with our experimental results, suggesting that this formalism can be used to compare the effects of co-doping of different single-phase compositions and concentrations.

Finally, we comment on the disparity that Raghavan et al. [1] noted between their thermal conductivity data for a rather similar equimolar co-doped composition and their expectation based on model they used for thermal conductivity. Raghavan et al. used Eq. (5), with a value for the parameter u given by:

$$u = \frac{100}{\sqrt{1.13}}(\Gamma/T)^{1/2} \tag{16}$$

(Eq. (7) of Ref. [1]) to compare with their data. Eq. (16) has the same functional dependence on temperature and atomic masses as Eqs. (6) and (8) above. Part of the discrepancy between their results and the predictions they made is undoubtedly due to having to use a value for the conductivity of defect-free zirconia, κ_I. This is a relatively poorly known quantity as good quality monoclinic zirconia is not readily available. As can be seen from the comparison between Eq. (5) and the data in Fig. 5b, the predicted thermal conductivity is consistently higher than the data and discernible temperature dependence is predicted at least up to about 500 °C. If Eq. (5) is used and the conductivity of defect-free zirconia adjusted so that the equation fits the data at high temperatures, then the conductivity of defect-free zirconia at 100 °C is calculated to be 3.1 W mK^{-1}. This compares with the value of 6.25 W mK^{-1} that Raghavan et al. used.

7. Conclusions

The thermal conductivities of "non-transformable" zirconia compositions formed by equimolar co-doping with either Y^{3+} and Ta^{5+} or Yb^{3+} and Ta^{5+} are very low (<2 W mK^{-1}) and nearly temperature-independent. The thermal conductivities of all the compositions are satisfactorily explained in terms of a defect scattering model that takes into account both a minimum phonon mean free path

and the mass disorder associated with the random substitution of the Y^{3+} or Yb^{3+} and Ta^{5+} ions on the cation lattice of the zirconia. The ratio of the conductivities of the Yb and Y trivalently doped compositions also scale with the inverse square root of the mass disorder scattering coefficients. As the atomic masses of the Y^{3+} and Nb^{5+} ions are similar, it can be expected that the "non-transformable" zirconia compositions formed by equimolar co-doping with Nb^{5+} instead of Ta^{5+} will have almost identical thermal conductivities to the equimolar Y^{3+}+Ta^{5+} compositions rather than the Yb^{3+}+Ta^{5+} compositions.

Acknowledgements

This work was supported by Honeywell Aerospace and the authors are grateful to Dr. W. Baker and V. Tolpygo for on-going discussions about these materials.

References

[1] Raghavan S, Wang H, Porter WD, Dinwiddie RB, Mayo MJ. Acta Mater 2001;49:169.
[2] Winter MR, Clarke DR. Acta Mater 2006;54:5051.
[3] Klemens PG. Physica B 1999;263–264:102.
[4] Garvie RC. J Mater Sci 1976;11:1365.
[5] Kim DJ, Jung HJ, Jang JW, Lee HL. J Am Ceram Soc 1998;81:2309.
[6] Kim D-J, Tien T-Y. J Am Ceram Soc 1991;74:3061.
[7] Leckie RM, Shen Y, Clarke DR, Levi CG. In preparation.
[8] Cairney JM, Rebollo NR, Ruhle M, Levi CG. Int J Mater Res 2007;98:1177.
[9] Klemens PG. Proc Phys Soc London Sect A 1955;68:1113.
[10] Klemens PG. Solid State Phys – Adv Res Appl 1958;7:1.
[11] Clarke LI, Taylor R. J Appl Phys 1975;46:714.
[12] Schlichting KW, Padture NP, Klemens PG. J Mater Sci 2001;36:3003.
[13] Kubascheski O, Alcock CB. Metellurgical thermochemistry. Oxford: Pergamon Press; 1979.
[14] Mevrel R, Laizet J-C, Azzopardi A, Leclercq B, Poulain M, Lavigne O, et al. J Eur Ceram Soc 2004;24:3081.
[15] Callaway J, von Baeyer HC. Phys Rev 1960;120:1149.
[16] Callaway J. Phys Rev 1959;113:1046.
[17] Berman R. Thermal conduction in solids. Oxford: Clarendon Press; 1976.
[18] Grimvall G. Thermophysical properties of materials. Amsterdam: North Holland; 1986.
[19] Slack GA. Phys Rev 1962;126:427.
[20] Maloney MJ. US patent; 2000.